

Relaxor Antiferroelectric Dynamics for Neuromorphic Computing

Dongliang Yang, Yinan Lin, Weifan Meng, Zhongyi Wang, Huihan Li, Ce Li, Zirui Zhang, Qianyu Zhang, Junqi You, Jiarui Wang, Tianze Yu, Yutao Li, Weiting Miao, Weili Zhen, Fei Xue, Ruixiang Fei, and Linfeng Sun*

Relaxor antiferroelectric (AFE) materials display a gradual polarization response and high energy storage density with polarization slowly reverting after removing an external field. This distinctive polarization-switching behavior closely resembles synaptic plasticity in biological nervous systems, presenting substantial potential for neuromorphic computing applications. Especially, its 2D scenario exhibits unique physical properties and maintains stability at atomic thickness due to their antipolar alignment, which effectively eliminates the depolarization field effect. Such stable 2D relaxor AFE materials offer significant advantages for integrating these materials into modern electronic devices for neuromorphic computing. In this study, the potential of a novel quaternary layered AFE material, $\text{CuBiP}_2\text{Se}_6$ (CBPS), is explored for neuromorphic device applications. CBPS exhibits a broad range of light absorption and stable relaxor AFE behavior, rendering it an outstanding candidate for optoelectronic synaptic devices. High-quality CBPS is synthesized and its AFE properties through various characterization techniques are verified. CBPS-based synaptic devices demonstrate dual-mode tunable resistance plasticity stimulated by both electrical and optical inputs, demonstrating the capacity to perform in-sensor computing for image restoration tasks. These findings suggest that relaxor AFE materials like CBPS could provide a robust platform for various brain-inspired applications, particularly in neuromorphic computing, and artificial visual systems.

domains can flip, allowing the material to exhibit ferroelectric (FE) behavior.^[1–6] Among various AFE materials, relaxor antiferroelectrics are particularly remarkable. Compared to conventional AFE materials, relaxor antiferroelectrics exhibit a more gradual polarization response and higher energy storage density under an applied electric field. Their uniqueness lies in the fact that, upon removal of the external electric field, polarization does not instantly collapse but instead slowly relaxes to its original state.^[7–12] This relaxation behavior of relaxor AFE materials differs significantly from the relaxation behaviors of traditional FE and AFE materials.^[13–17] This characteristic makes relaxor AFE materials ideal candidates for mimicking synaptic plasticity in neuromorphic computing. However, traditional AFE materials face fatigue and aging phenomena during prolonged operation, which in turn affect the lifespan and reliability of devices.^[18] Additionally, influenced by size effects, dangling bonds, and interface effects, it is challenging to meet the development demands for device miniaturization while ensuring satisfactory device performance.^[19–21]

1. Introduction

Antiferroelectric (AFE) materials possess unique properties, with antiparallel dipole arrangements and nearly zero remnant polarization. However, when an electric field is applied, these electric

2D van der Waals (vdW) FE/AFE materials, with their excellent optoelectronic properties and the advantage of having no dangling bonds on the surface, have become an ideal choice for constructing neuromorphic chips.^[22] Among numerous such kinds of material systems, thiophosphates and

D. Yang, Y. Lin, W. Meng, H. Li, C. Li, Z. Zhang, Q. Zhang, J. You, J. Wang, T. Yu, Y. Li, W. Miao, W. Zhen, R. Fei, L. Sun
Centre for Quantum Physics
Key Laboratory of Advanced Optoelectronic Quantum Architecture and Measurement (MOE)
School of Physics
Beijing Institute of Technology
Beijing 100081, P. R. China
E-mail: sunlinfeng@bit.edu.cn

D. Yang, Y. Lin, W. Meng, H. Li, C. Li, Z. Zhang, Q. Zhang, J. You, J. Wang, T. Yu, Y. Li, W. Miao, W. Zhen, R. Fei, L. Sun
Beijing Key Lab of Nanophotonics & Ultrafine Optoelectronic Systems
School of Physics
Beijing Institute of Technology
Beijing 100081, P. R. China
Z. Wang, F. Xue
Center for Quantum Matter
School of Physics
Zhejiang University
Hangzhou 310027, P. R. China

The ORCID identification number(s) for the author(s) of this article can be found under <https://doi.org/10.1002/adma.202419204>

DOI: 10.1002/adma.202419204

selenophosphates, which are wide-bandgap dielectric materials with the ABP_2X_6 structural form, have attracted particular attention.^[23–29] In these compounds, X typically represents a chalcogen (e.g., S, Se, Te), while A and B are metal ions that may occur in monovalent/trivalent or divalent/divalent combinations. The layered structure of these materials results from the organization of $[(\text{PX}_3)-(\text{PX}_3)]^{4-}$ anions, arranged with P–P bonds aligned in a “bed of nails” configuration, flanked by two parallel “sheets” of X atoms.^[30,31] Between these sheets, A and B metal ions occupy quasi-octahedral voids formed by X atoms from adjacent anions. A defining characteristic of these materials is the behavior of the A and B metal ions within the octahedral sites: they may reside centrally, creating a hexagonal, paraelectric structure with no net dipole moment, or shift asymmetrically towards one X plane, inducing a vertical local polarization. Within a layer, these dipole moments may align ferroelectrically, antiferroelectrically, or in random orientations, contributing to phase transitions within the material layer.^[25,27]

To date, research on layered thiophosphate and selenophosphate materials for neuromorphic computing has predominantly focused on CuInP_2S_6 ^[32–34] and CuCrP_2S_6 .^[17,35,36] For example, Sun et al. reported a high-performance memristor^[37] based on ionic 2D CuInP_2S_6 , detailing its potential for neuromorphic computing, including continuous linear conductivity changes, low operating current, device uniformity, and performance in pattern recognition and complex signal transmission. Wang et al. designed a ferroelectric field-effect transistor (Fe-FET) based on the full 2D $\text{SnS}_2/\text{h-BN}/\text{CuInP}_2\text{S}_6$ structure,^[38] achieving excellent storage performance and multifunctional sensing-memory-computing visual simulations through light-induced ferroelectric polarization reversal. Additionally, Ma et al. studied high-performance memristors^[17] based on the van der Waals AFE material CuCrP_2S_6 , which exhibited a high resistance switching ratio, excellent cycling endurance, and strong thermal stability, capable of simulating biological synaptic learning rules. Although CuInP_2S_6 and CuCrP_2S_6 have shown promising results, achieving both optical and electrical synaptic behaviors simultaneously in a single material with high performance (retention time, operation voltage, power consumption, etc.) remains a challenge. In many existing materials, optical and electrical responses are typically separate, requiring different materials or structures to handle electrical synaptic behavior and optical synaptic behavior independently. This not only increases the complexity of the device but also limits its integration density and stability. $\text{CuBiP}_2\text{Se}_6$ (CBPS), as an emerging selenophosphate, exhibits outstanding AFE properties^[27,39,40] and broad-spectrum optical responsiveness,^[41] making it uniquely promising for applications in multimode neuromorphic computing and bio-inspired visual systems. In this work, we synthesized high-quality CBPS single crystals of quasi-centimeter size using the chemical vapor transport (CVT) method, confirming their high purity and precise atomic structure through multiple characterization techniques. Moreover, through ferroelectric characterization, we demonstrated that CBPS exhibits AFE behavior at room temperature, enabling polarization reversal controlled by external electric fields to simulate synaptic learning and memory processes. Furthermore, the fabricated CBPS-based two-terminal horizontal devices exhibited symmetry and nonlinear current response characteristics, akin to the synaptic plasticity of biological

neurons. These devices are capable of simulating key biological synaptic characteristics, including paired-pulse facilitation (PPF), long-term potentiation (LTP), and long-term depression (LTD). Additionally, CBPS materials exhibit outstanding optoelectronic properties, functioning effectively across a broad wavelength range. Through optical stimulation, CBPS devices can replicate PPF behavior observed in biological systems and facilitate transitions from short-term memory (STM) to long-term memory (LTM). Finally, the CBPS devices were employed in-sensor computing for image restoration tasks. By training a generative adversarial network (GAN), CBPS was functions as a photosensitive encoder to extract features from incomplete visual inputs, while the decoder, composed of an artificial neural network, was tasked with generating the missing regions. In hardware system experiments, we validated the performance of the generative model, which demonstrated high overall writing accuracy despite noise and writing errors. This research on relaxor AFE materials like CBPS suggests that CBPS-based devices offer broad application prospects in neuromorphic computing and brain-like visual systems.

2. Results and Discussion

Here, we constructed a neuromorphic computing device using CBPS that achieves multifunctional integration by responding to external stimuli such as light and electrical signals. CBPS functions as the core active layer, simulating the synaptic cleft, while two electrodes emulate the presynaptic and postsynaptic membranes. When exposed to light or electrical stimuli, the CBPS layer leverages its antiferroelectric and photoreceptive properties to perform signal transmission and processing similar to biological synapses. Furthermore, the CBPS device is applied to in-sensor computing for image inpainting, where CBPS acts as the encoder to detect optical signals and extract latent features of the incomplete image, while the memristor chip serves as the decoder to ultimately achieve image inpainting functionality in the experiment, as shown in **Figure 1a**. This capability enables the emulation of complex synaptic behaviors, highlighting the potential of CBPS in neuromorphic computing and image processing applications. We synthesized high-quality quasi-centimeter-sized CBPS single crystals (inset in **Figure 1b**) using CVT methods (synthesis methods are detailed in **Figure S1**, Supporting Information). The micro-X-ray diffraction (XRD) results of the synthesized CBPS crystals matched well with previously reported data,^[41] confirming the high purity phase of the sample (**Figure 1b**). Additionally, the Raman spectra of the CBPS thin layers were measured using a 532 nm laser with a laser power of 0.5 mW. The peaks E_g^1 , E_g^2 , A_g^1 , A_g^2 , A_g^3 are located at 111.7, 135.3, 207.5, 431.9, and 465.9 cm^{-1} , respectively, aligning with previously reported experimental results.^[41] (**Figure 1c**).

Furthermore, we investigated the atomic structure of few-layer CBPS using high-angle annular dark field (HAADF) scanning transmission electron microscopy (STEM), observing precise structural matching and different brightness points (**Figure 1d**). The atomic ratio of the synthesized CBPS, determined by energy-dispersive X-ray spectroscopy (EDX), corresponds well with the stoichiometric ratio of 1:1:2:6 for Cu:Bi:P:Se (see **Figure S2**, Supporting Information). The chemical composition and oxidation

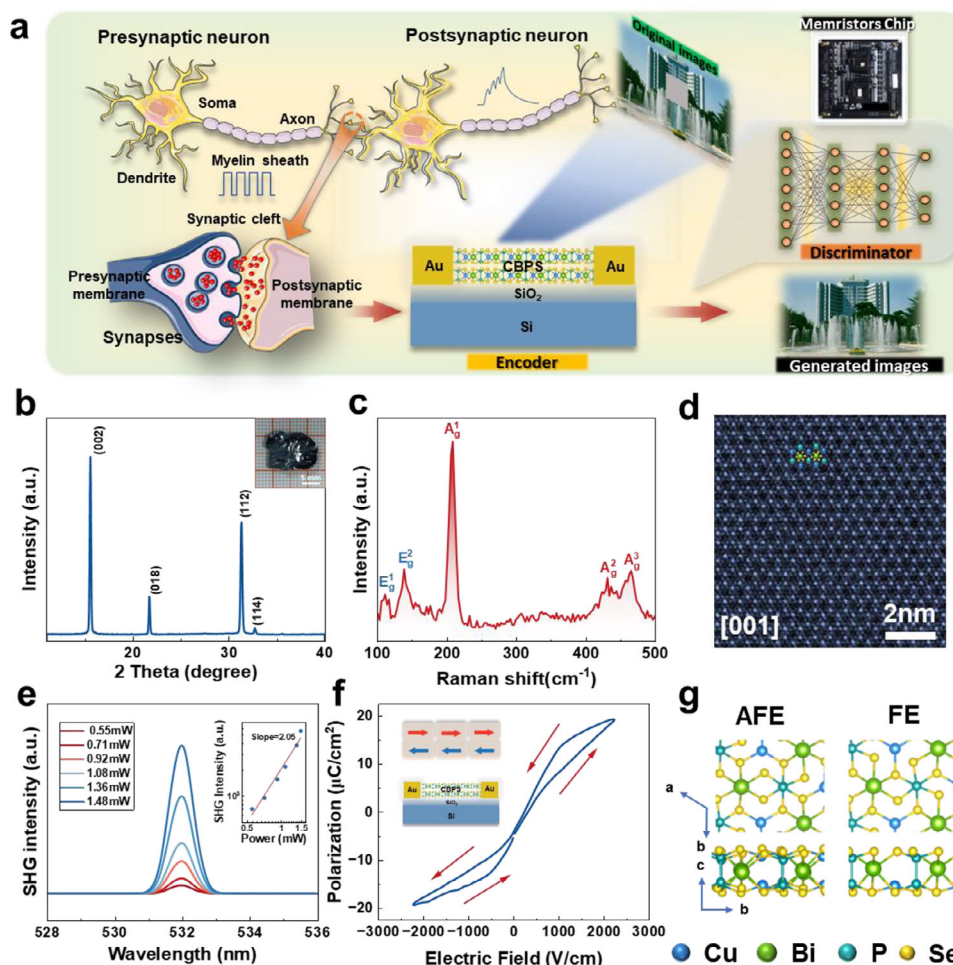


Figure 1. Synthesis and Characterization of 2D CuBiP₂Se₆. a) A schematic diagram of using CBPS devices to simulate biological synapses for image restoration. b) XRD of CBPS. The insert is optical image of the quasi-centimeter size CBPS single crystal. c) The Raman spectrum of CBPS. d) STEM image of CBPS. e) SHG spectra of CBPS. Inset is the excitation power dependence of the SHG intensity in logarithmic coordinates. f) *P*–*E* hysteresis loops measured on CBPS ferroelectric capacitor. g) Top and sectioned side views of CBPS monolayers, where Cu is in blue, Bi is in green, Se is in yellow, and P is in dark green.

states of CBPS were further confirmed using X-ray photoelectron spectroscopy (XPS). High-resolution XPS spectra revealed characteristic peaks: Cu2p_{1/2} (952.48 eV), Cu2p_{3/2} (935.58 eV), Bi4f_{5/2} (163.45 eV), Bi4f_{7/2} (158.15 eV), P2p_{1/2} (132.1 eV), P2p_{3/2} (131.2 eV), Se3d_{3/2} (54.95 eV), and Se3d_{5/2} (54.1 eV), which are attributed to Cu⁺, Bi³⁺, P⁴⁺, and Se²⁻ ions, respectively (see Figure S3, Supporting Information). Due to the displacement of Cu ions in the crystal lattice, CBPS adopts a non-centrosymmetric structure, enabling strong second-harmonic generation (SHG). SHG measurements of CBPS nanoflakes were carried out using a 1064 nm excitation laser at varying excitation powers. The SHG signals increase with the incident excitation power, and the SHG intensity follows a standard quadratic relationship with the excitation power. The ideal coefficient of 2.05 consistent with the predictions of electric dipole theory.^[42] (Figure 1e). According to previous reports, CBPS exhibits an AFE phase at room temperature. To this end, we prepared two-terminal horizontal devices using mechanically exfoliated CBPS. The thickness of the nanosheets was 8 nm, characterized by atomic force mi-

croscopy (AFM) (Figure S4, Supporting Information). The room-temperature *P*–*E* hysteresis loop of CBPS was measured to confirm its AFE behavior, as presented in Figure 1f. It was observed that an external electric field induces a polarized state in CBPS (also called field-induced FE state). The polarization returns to zero once the applied electric field is removed, demonstrating its relaxor AFE behavior. Moreover, AFE phase of CBPS remains stable even when the thickness is thinner (Figure S5, Supporting Information). In the AFE phase, the Cu atoms in adjacent layers are either closer together or farther apart than the interlayer distance. In contrast, in the FE phase, all Cu atoms are located either at the top or the bottom of each layer to represent polarization, as shown in Figure 1g. In AFE materials, adjacent electric dipoles are arranged in an antiparallel manner, resulting in a macroscopic polarization strength of zero. However, in CBPS, we observed a small but nonzero negative remanent polarization. According to the bond charge model,^[25,43,44] a potential difference exists between the different ions in each bond, which can induce a shift in the bond charge center. This shift leads to a deviation

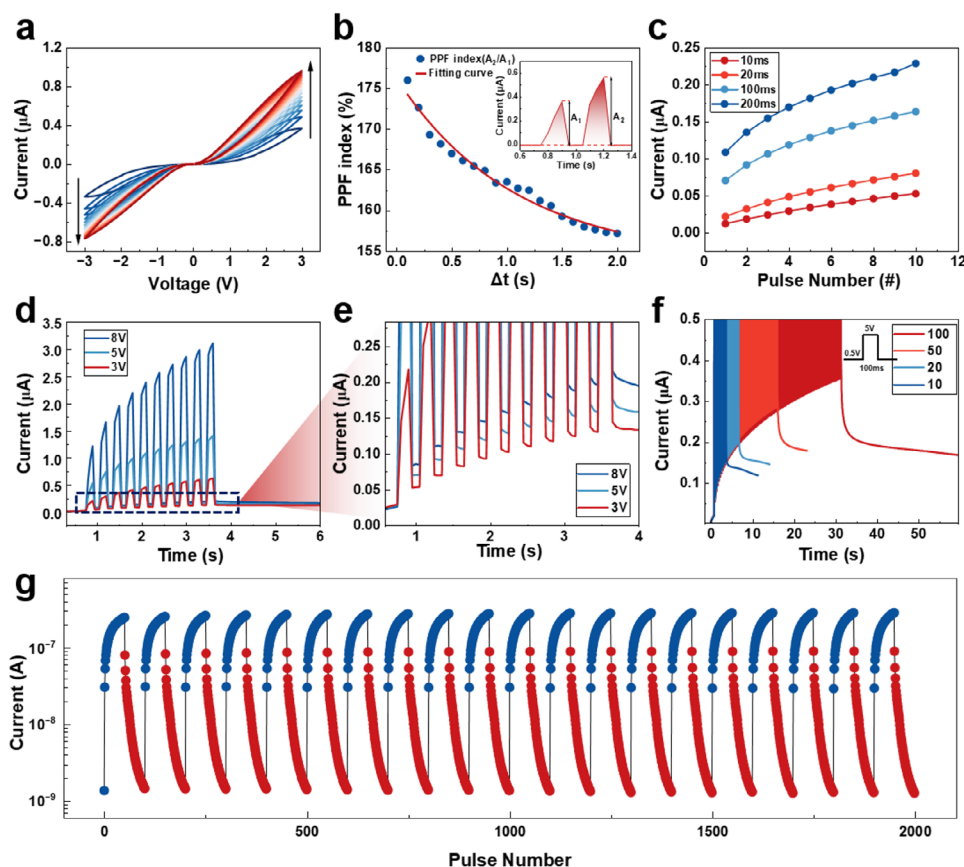


Figure 2. Electrical measurements of the CBPS device. a) I - V curve of CBPS device. b) PPF index as a function of electric pulse interval time Δt . c) Changes in post-synaptic current by applying voltages of varying pulse widths. d) Changes in post-synaptic current by applying voltages of varying pulse amplitude. e) The magnified area of the red square in (d). f) Changes in post-synaptic current by applying voltages of varying pulse number. g) Stable potentiation/depression cycle (pulse amplitude of $V_{pre} +5$ V and $V_{dep} -3$ V, pulse width of 100 ms, reading voltage of 0.5 V).

in the ideal antiparallel dipole arrangement, generating spontaneous polarization and ultimately accounting for the observed phenomenon. (More device fabrication details in the Experimental Section)

With the experimentally confirmed AFE behavior of CBPS, its polarization reversal can be controlled by external electric fields to emulate synaptic learning and memory processes. **Figure 2a** presents the current-voltage (I - V) curves of the device, with the voltage sweep sequence set to 0—3 V—0 V—3 V—0 V. As the number of positive and negative voltage sweeps increases, the channel current gradually rises, exhibiting a symmetric and nonlinear response under both bias polarities. This behavior is primarily attributed to the flipping of internal electric domains under the influence of the electric field, which leads to alterations in the polarization state of this material and, consequently, variations in current. Upon removal of the applied electric field, the electric domains in CBPS revert to their original configuration owing to the AFE behavior. We also examined the I - V curves at different voltage sweep ranges (± 1 V and 5 V). It is evident that as the voltage range diminishes, the I - V curves reflect a corresponding reduction in current response. This indicates that at lower voltages, the applied electric field is inadequate to significantly impact the flipping process of the electric domains within the CBPS material. Since the driving force on the electric domains is

weak at lower voltages, the changes in polarization state are minimal, resulting in a relatively subdued current response. In contrast, when the voltage range is increased to ± 5 V, the I - V curves exhibit a more pronounced current response. This is due to the fact that at higher voltages, the applied electric field is sufficiently strong to induce more vigorous flipping of the electric domains within the CBPS material. At elevated voltages, the energy barrier for domain flipping is effectively reduced, allowing a greater number of domains to respond to variations in the applied electric field, thereby enhancing the current response of device. Furthermore, as the voltage range increases, the electric domains in CBPS are more inclined to undergo complete flipping and reorientation under the applied electric field, potentially resulting in greater remnant polarization effects. This observation suggests that upon removal of the electric field, the domains may not entirely revert to their original stable states, leading to a degree of hysteresis in the I - V response. (see Figure S6, Supporting Information). During each scanning cycle, the applied electric field influences the domain structure within the material. With repeated cycling, the electric domains become more ordered, which enhances the efficiency of domain switching during subsequent field applications. This increase in domain switching efficiency leads to a gradual rise in current. Additionally, as the scanning cycles increase, some domains may align in favorable directions,

resulting in the gradual accumulation of polarization in the material. This accumulation effect makes polarization reversal easier in subsequent cycles, thereby leading to an increase in current. We further verified this phenomenon through continuous piezoresponse force microscopy (PFM) scanning. Experimental results indicate that as the scanning cycles increase, both the PFM phase and amplitude signals undergo significant changes, demonstrating the dynamic evolution of polarization domains. In the initial state, the PFM phase contrast is weak. However, after the application of an electric field, the domains begin to switch and gradually become more ordered. Additionally, the enhancement of the PFM amplitude signal indicates an increase in local piezoelectric response, which is closely related to the polarization accumulation effect. This further supports the evolution of polarization domains under continuous electric field application, as shown in Figure S7 (Supporting Information).

Due to the small size of Cu^+ ions, the $[\text{BiP}_2\text{Se}_6]^-$ anions tend to form a 2D structure and strongly traps the Cu^+ ions within the octahedral coordination environment formed by Se atoms. As demonstrated by Gave et al.,^[27] the actual positions of Cu^+ ions are disordered and located in various off-center positions. This unique structural feature enables the displacement of Cu^+ ions within the selenium octahedra when a horizontal electric field is applied. This movement leads to a change in the local polarization vector, which then reorients the in-plane dipoles and ultimately results in domain switching. During the electric field cycling, when the field gradually decreases from its maximum positive value to zero, the Cu^+ ions do not immediately return to their initial positions attributed to the strong interaction between the Cu^+ ions and $[\text{BiP}_2\text{Se}_6]^-$ anions, combined with the constraints imposed by their disordered positions. As a result, the domains partially retain the modified state, and the material's conductivity differs from the initial state. The reversible flipping characteristics of the electric domains under an applied electric field and their responses to different voltage ranges closely resembles the synaptic plasticity of biological neurons,^[45–49] wherein the strength and pattern of synaptic signal transmission change under varying stimulus intensities. This behavior is crucial for realizing synaptic plasticity in neuromorphic computing, particularly in devices designed for biomimetic memory functions. The symmetry and nonlinear current response characteristics of CBPS materials enable effective simulation of nonlinear transmission functions in synapses, thereby enhancing the computational capability of neuromorphic devices. The PPF reflects a phenomenon of short-term synaptic plasticity, revealing dynamic changes in the mechanisms of calcium ion entry and vesicle release during synaptic transmission.^[50–53] When the first spike is applied, calcium ions enter the presynaptic terminal. While some calcium ions are cleared, a portion remains within a short time interval. As the second spike is stimulated, these residual calcium ions accumulate with new calcium ions entering, increasing the probability of vesicle release, thereby leading to a stronger synaptic response to the second spike.

Figure 2b shows two successive 5 V pulses (100 ms width) applied to the device, followed by a read voltage of 0.5 V. The ratio of the excitatory postsynaptic current induced by the second pulse to that induced by the first pulse is defined as the PPF index. Furthermore, by measuring a series of dual-pulse voltage-induced reactions at different time intervals (Δt) and calculating the ratio A_2

to A_1 , the results indicate that the maximum PPF index reaches 176%, occurring at a short interval of 10 ms, gradually decreasing to 156% as the interval increases to 2 s. The decay curve can be well-fitted using a double exponential function,^[51] comparable to the characteristics of PPF in biological synapses. In addition, both the width and frequency of pulse signals play critical roles in encoding and transmitting information during neural signal transmission in biological synapses. In experiments, we observed remarkable changes in post-synaptic current by applying voltages of varying pulse widths. As Figure 2c shows, the synaptic device's response current increases gradually as the pulse width grows. Figure 2d presents current variations where different amplitude pulse voltages were applied to stimulate the synaptic device ten times, with each pulse width set to 100 ms. Such significant current changes in synaptic weight under different pulse voltages have important implications for simulating the plasticity of biological synapses.^[22,54–56] As illustrated in Figure 2e, the current of the device shows gradual relaxation behavior after the pulse voltage (spike) is removed, which is related to remnant polarization in CBPS. Moreover, the biological synapses adjust their connection strength by receiving different numbers of neural pulses.^[57,58] Therefore, we also measured the current response of the synaptic device after applying different pulse counts to simulate such biological characteristics, shown in Figure 2f. It is evident that a higher number of pulses leads to a greater adjustment in synaptic weight, which is crucial for simulating the learning and memory functions of biological synapses. LTP and LTD are two significant indicators for assessing the accuracy of pattern recognition in neural network simulations. The optimal pulse scheme for LTP/LTD involves applying 50 pulses, with V_{pre} set to +5 V and V_{dep} to -3 V, each pulse having a width of 100 ms, as exhibited in Figure 2g. The device performance remains stable over 20 cycles under both positive and negative stimuli, with a simulated switching ratio exceeding 100 times. In Figure S8 (Supporting Information), we also measured the device over 20 cycles with 20 pulses, showing greater stability and performance compared to other LTP/LTD inducing devices. In addition, we quantitatively analyzed the impact of polarization recovery on memory performance and found that even under high voltage conditions, the decay process is relatively slow. This characteristic enhances the storage performance of the device, providing an advantage for long-term information retention in Figure S9 (Supporting Information).

Moreover, sensing is important in bioinspired neuromorphic computing, as it directly mirrors the human visual system, where more than 80% of information about the external environment is acquired through light-based stimuli.^[59,60] In the human visual system, light enters the retina through the eye, where photoreceptor cells (rods and cones) convert optical signals into neural signals, which are then transmitted through the optic nerve to the visual cortex of the brain for processing and decoding. During this process, the human visual system demonstrates sensitivity to light intensity, color, and motion, utilizing complex neural networks to perceive and compute external visual information.^[61–65] CBPS materials exhibit promising characteristics as artificial light-sensitive synaptic materials for mimicking the neural signal processing and transmission of the visual system.^[41] Consequently, we design the two-terminal photosensitive AFE devices based on the CBPS flakes to simulate the human visual system.

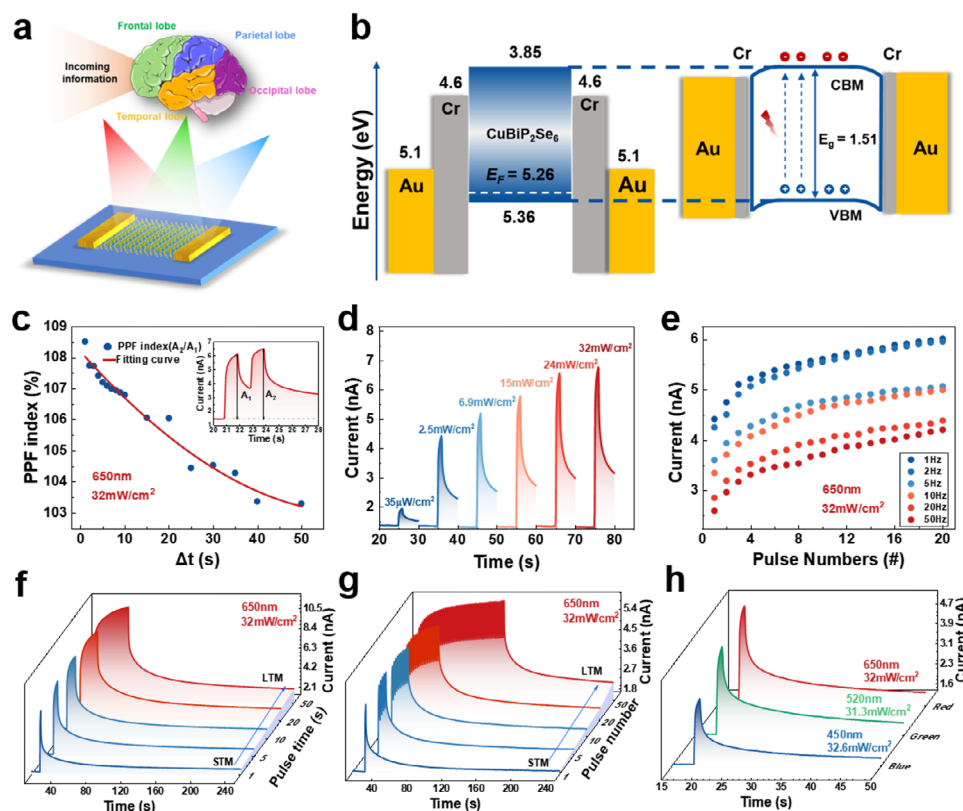


Figure 3. Optical measurements of the CBPS device. a) Schematic diagram of CBPS photoelectric synaptic device. b) Energy level and energy band alignment diagrams of the CBPS photoelectric synaptic device. c) PPF index as a function of optical pulse interval time Δt . Changes in post-synaptic current by applying optical stimulation of different d) power, e) frequency, f) time, g) number and h) wavelength.

Figure 3a illustrates the perception and processing of information in the biological visual system, along with a schematic of the photosensitive AFE device structure. The full energy band diagram of the CBPS device before contact is presented on the left side of Figure 3b. After contact, due to the difference in the Fermi levels of the metal and CBPS, electrons are injected from the metal into CBPS until their Fermi levels reach thermal equilibrium, leading to the formation of a space charge region in CBPS.

This causes the valence band and conduction band at the contact interface to bend downward relative to the energy bands in the bulk CBPS, aligning the Fermi levels of the metal and CBPS, as shown on the right side of Figure 3b. Similar to the above electrical stimulation, we used optical stimulation to simulate PPF in biological systems. During the initial illumination, the carriers trapped by the traps will change the internal electric field distribution of the material. After the second illumination generates new carriers, the carriers in the traps will be released and act together with the newly generated carriers, amplifying the response to the subsequent stimuli, thus exhibiting the PPF behavior. As illustrated in Figure 3c, the device does not quickly return to its initial state after optical stimulation, due to the presence of surface states and defect states that can trap the charge carriers generated by the light stimulation, delaying the recovery of the resistance of material to its initial state. By varying the pulse interval (Δt) from 0.1 to 50 s, the results indicate that the maximum PPF index is 108%, occurring at a short interval of 0.1 s. A double-exponential

function fits the decay curve well, also demonstrating the potential to simulate PPF in biological systems.

The relationship between a single optical spike and post-synaptic current, along with light power density (P), is illustrated in Figure 3d. As P increases (650 nm, duration 1 s), post-synaptic current progressively rises, attributed to the increased photogenerated charge density in CBPS, where captured charges at the interface are excited and released into the conductive channel. When using optical pulses (650 nm, $P = 32 \text{ mW cm}^{-2}$) to simulate the memory process, lower post-synaptic current levels were achieved as the pulse frequency increased from 1 to 50 Hz, as depicted in Figure 3e. Moreover, the learning and memory processes of the human brain can also be simulated through optical modulation, differentiating memory types into STM and LTM. By altering the duration and quantity of optical pulses, transitions from STM to LTM can be achieved, as demonstrated in Figure 3f,g. Given that CBPS can operate across a wide wavelength range, we measured the responses of the photosensitive device to green (520 nm) and blue light (450 nm), in consistency with responses to red light in Figure 3h. This suggests that CBPS devices possess greater potential and application value in perceiving, processing, and responding to complex optical environments. We also add more responses of the device to green and blue light at various laser frequencies, power density, durations, and pulse counts (Figures S10 and S11, Supporting Information). To more thoroughly demonstrate the superior performance of

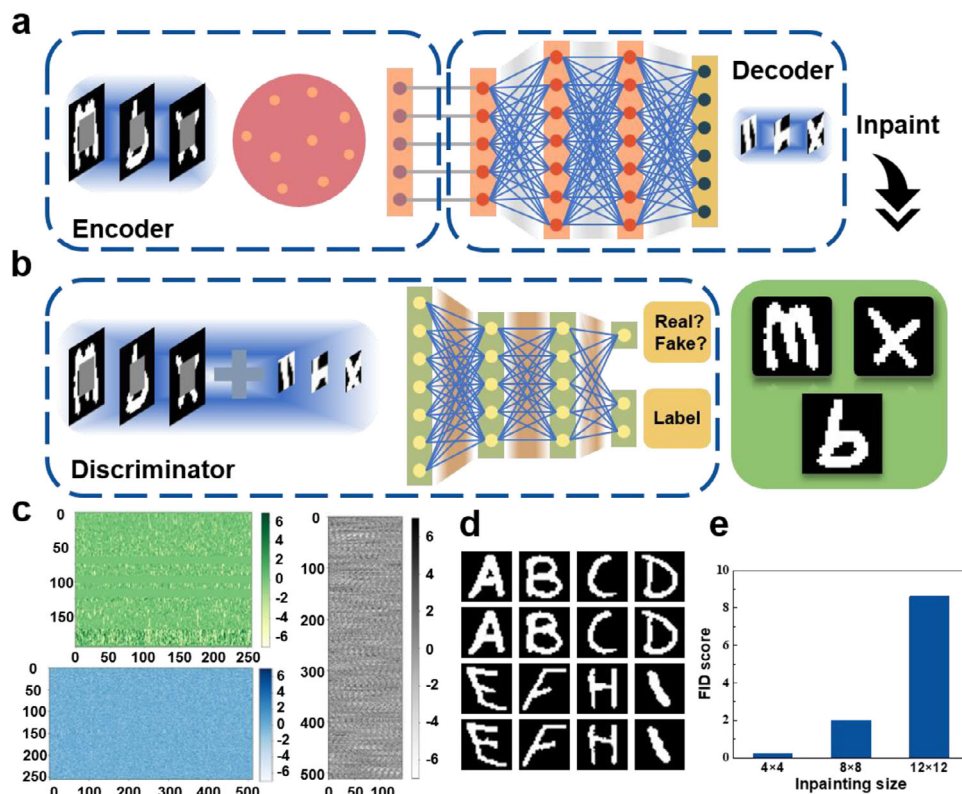


Figure 4. Simulation of CBPS based in-sensor encoder for image inpainting. a) Schematically illustration of the image generation model of the GAN. Left panel: CBPS based dynamic encoder to obtain features. Right panel: memristors based decoder for features processing and produces the missing regions. b) The discriminative model of GAN for image classification which tries to distinguish the generation image. c) The trained quantization weight matrix of decoder (olive drab matrix, blue matrix and gray matrix represent the 1st, 2nd and 3rd layer respectively). d) Simulation results of the generation model. The first and third rows show the original images, and the second and fourth rows show the inpainting images. e) FID score for evaluating GAN. The smaller the score, the better the quality of the generated images.

CBPS, we have compared it with related works, as shown in Table S1 and Figure S12 (Supporting Information). Through this comparison, we found that, compared to some three-terminal structures, CBPS not only has an ultrathin thickness of only 6 nm, but its device structure is also simpler, with comprehensive performance. Additionally, CBPS enables synaptic behavior with both light and electrical stimuli within a single material. While other materials also have light or electrically driven modes, this dual-response characteristic of CBPS provides an advantage in simulating biological synaptic functions. Furthermore, CBPS can operate under various wavelengths, including 650, 520, and 450 nm, indicating its broader applicability to different colors or frequencies of light signals. In terms of energy consumption, CBPS devices also exhibit low energy consumption—11.7 pJ (electrical) / 0.88 pJ (optical). Additionally, CBPS devices exhibit excellent retention.

The photosensitive AFE device is employed for in-sensor computing in an image inpainting task. Given an image with missing region, a GAN is trained to regress the missing pixel values.^[66] Figure 4 illustrates the simulation results and proposed network architecture is shown in Figure 4a,b. In this task, we conducted experiments using the EMNIST dataset.^[67] First, the central region of the image was removed, and the remaining image was encoded into optical pulses (the 28×28 image is cropped into

196-wide 4-long optical image). The CBPS served as a photosensor to detect the optical signals and extract the latent features of the incomplete image. It is called encoder, shown in left panel in Figure 4a.

The right panel in Figure 4a illustrates a decoder consisting of an artificial neural network with two hidden layers to produce the missing region. These two components form the generative model for this task. To achieve better inpainting results, we introduced a discriminator model and jointly trained the generative model using the adversarial loss and reconstruction loss. Figure 4c shows the three-layer weight matrices of the decoder from the software simulation, with the weights quantized to 4 bits to facilitate subsequent hardware experiments with memristors. The olive drab matrix, blue matrix, and gray matrix represent the 1st, 2nd and 3rd layer respectively. Figure 4d exhibits partial comparison between the inpainting images (first and third rows) and the original images (second and fourth rows). It is shown that even with a 4-bit decoder, the images can be restored effectively. To further evaluate the performance of the generative model, we calculated the Frechet inception distance (FID) between the generated images and the original images. FID score was proposed and used by Heusel et al.^[68] A lower FID score indicates a higher quality of the generated images. We compared the impact of different sizes of the missing central region on image completion

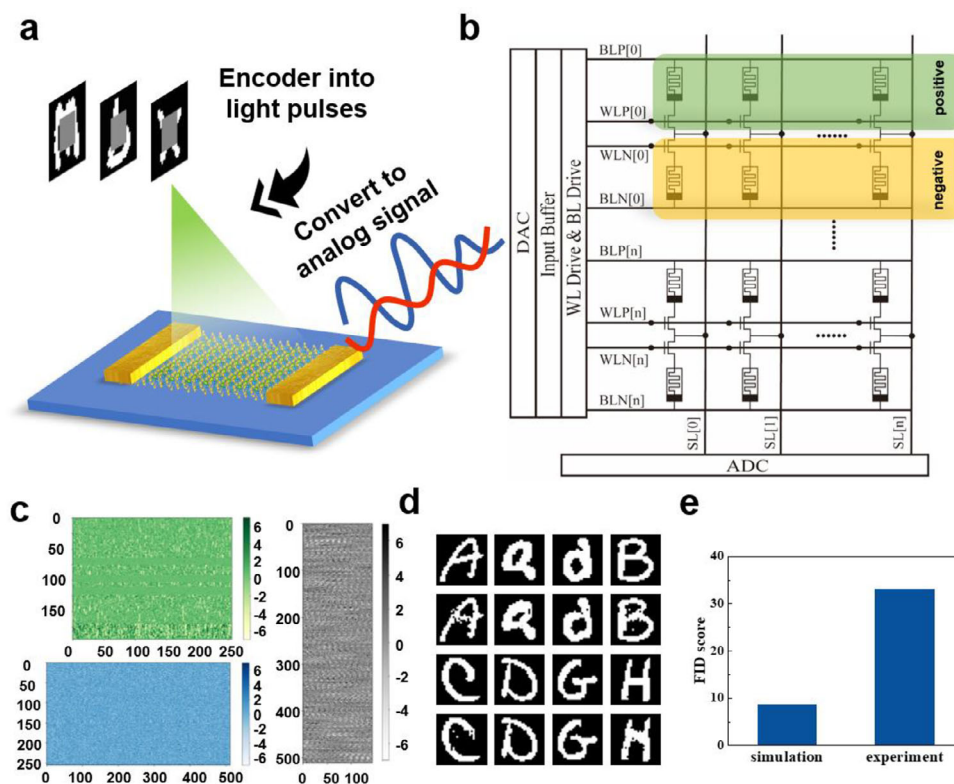


Figure 5. Experiment of CBPS based in-sensor encoder for image inpainting. a) Schematically illustration of the incomplete images is programmed as light pulses and read the response current of the CBPS device. (Encoder part in Figure 4a) b) Schematic diagram of fully-integrated computing-in-memory chip. The chip is composed of a sign-weighted 2T2R memristors array, input/output buffers, ADCs, etc. c) The weight matrix read out after writing into the memristor array during the experiment. (olive drab matrix, blue matrix and gray matrix represent the 1st, 2nd and 3rd layer respectively). d) Experiment results of the generation model. The first and third rows show the original images, and the second and fourth rows show the inpainting images. e) FID score for evaluating GAN. A comparison of experiment and simulation with inpainting size of 12×12 is shown in graph.

performance by calculating the FID scores for three cases: 4×4 , 8×8 , and 12×12 (Figure 4e). The results indicate that even with a 12×12 missing region, the performance of inpainting is achieved.

We conducted experiments on the hardware system to validate the performance of the generative model. Using the same data preprocessing method as in the simulation, we obtained the optical response analog signals of the CBPS, as shown in Figure 5a. Figure 5b schematically illustrates the two-transistor two-memristor (2T2R) memristor array used in this experiment. In the 2T2R array, the positive weight and negative weight in a differential device pair are connected on the same output column. An x-bit signed weight value can be stored in a 2T2R cell. The weight matrices of the decoder obtained from the simulation is written into the array, and the weights are read from each position to obtain the matrices shown in Figure 5c. The color information is consistent with that in Figure 4c. The comparison of these two figures indicates that, despite some errors occurring during the writing process, the overall writing accuracy is still high, and the resulting matrices are largely consistent with the weight matrices obtained from the simulation. After statistical analysis, the final writing weights accuracy reached 84.56%. Figure 5d exhibits partial comparison between the experimental inpainting images (first and third rows) and the original images (second and fourth rows). Figure 5e compares the FID scores obtained

from experiments and simulations. Due to noise and writing errors, the FID parameter obtained experimentally is relatively higher.

3. Conclusion

In conclusion, relaxor AFE materials such as CBPS synthesized in this study exhibits unique AFE and optoelectronic properties, making it an ideal candidate material for neuromorphic computing and artificial synaptic devices. Our study demonstrates that CBPS can analogously replicate synaptic plasticity through reversible polarization switching under electrical stimulation while also extending its functionality by responding to a broad spectrum of optical stimuli. These capabilities enable CBPS devices to simulate key characteristics of biological synapses for image restoration tasks within sensor-internal computations. By training a GAN, CBPS functions as a photodetector to extract latent features from incomplete images, while the artificial neural network decoder is utilized to generate missing regions. Despite the presence of noise and writing errors in hardware system experiments, the overall writing accuracy remains high, validating the performance of the generative model. This research lays the groundwork for future exploration of the integration of relaxor AFE materials in advanced neuromorphic computing and multifunctional optoelectronic systems, which opens new avenues

in fields that require robust signal processing and adaptable learning behaviors, including in-sensor computing, high-fidelity image restoration, and advanced neuromorphic vision systems.

4. Experimental Section

Synthesis of $\text{CuBiP}_2\text{Se}_6$ Crystals: High quality quaternary $\text{CuBiP}_2\text{Se}_6$ single crystals were synthesized via high chemical vapor transport (CVT). Stoichiometric amounts of high-purity (all 99.99%) Cu, Bi, P, and Se were sealed in an evacuated 20 cm quartz ampule at 10^{-6} Torr and heated in a furnace. From ambient conditions, the temperature was increased to 870 °C within 48 h and held for ≈ 7 d. After heating, the furnace was allowed to cool to room temperature, upon which high-quality quaternary $\text{CuBiP}_2\text{Se}_6$ single crystals were obtained (Figure 1b; Figure S1, Supporting Information, was increased).

Characterization of $\text{CuBiP}_2\text{Se}_6$: The crystal structure of quaternary $\text{CuBiP}_2\text{Se}_6$ was characterized using micro-XRD (Bruker D8 Discover). The elemental valence state of quaternary $\text{CuBiP}_2\text{Se}_6$ was characterized by X-ray photoelectron spectroscopy (XPS, PHI VersaProbe III). The elemental distribution of quaternary $\text{CuBiP}_2\text{Se}_6$ was characterized using a Quanta 400. The Raman spectra were performed by the WITec alpha300 Raman system with an excitation laser of 532 nm. SHG characterization was measured by the WITec alpha300 Raman system using 1064 nm excitation. The STEM image was acquired by double aberration corrected TEM under 300 kV (Thermo Fisher Scientific, Titan Themis Z). The PFM measurements were performed using the Asylum Research MFP-3D and Cypher.

Device Fabrication: The atoms-thick $\text{CuBiP}_2\text{Se}_6$ were mechanically exfoliated from bulk crystals and transferred to a silicon substrate with a 285 nm thick SiO_2 layer via the dry transfer method using polydimethylsiloxane (PDMS). Devices were fabricated by electron-beam lithography (DZS500). The corresponding Cr/Au (5 nm/45 nm) electrodes were deposited by thermal evaporator (DM 400).

Device (Opto)electronic Measurement: (Opto)electronic measurements were performed under ambient vacuum conditions using a Keithley 4200A-SCS and Keithley 2636B semiconductor parameter analyzer in a probe station (CRX-6.5, LakeShore). The ferroelectric measurement was performed by ferroelectric analyzer (Huaace FE-2000 Analyzer) in a probe station (CRX-6.5, LakeShore). Monochromatic tunable-power lasers of 405, 532, and 635 nm were used to investigate the photoresponse of the quaternary $\text{CuBiP}_2\text{Se}_6$ -based device.

Simulations: For the image inpainting task, CBPS device functions as a nonlinear encoder, while an artificial neural network with two hidden layers (256 and 512 hidden neurons, respectively) serves as the decoder. The center-cropped Extended Modified National Institute of Standards and Technology (EMNIST) dataset as the input data, comprising 124 800 training images and 20 800 testing images. The current responses were collected after every four optical pulses so that the 196 current values were collected for each 28×28 image. The cross-entropy loss (CE), mean squared error loss (MSE) and binary cross-entropy loss (BCE) are jointly minimized by batch gradient descent using the Adam optimizer (initial learning ratio = 0.0005, step size = 20, gamma = 0.8). The reconstruction loss is, and the adversarial loss is, where CE_{real} and BCE_{real} refer to CE and BCE of original images, CE_{fake} and BCE_{fake} represent CE and BCE of generated images. After training, the model weights were quantized to 4-bit for subsequent inference and on-chip experiments with memristors.

Experiments: The experiment was conducted on a custom-designed system featuring two memristor chips on the with two 576×128 2T2R memristor array. The quantized, trained weights of decoder were mapped onto the memristor array. Current response values from the test images were converted into digital voltage vectors and multiplied by the quantized 4-bit weights. The output results were converted back into voltage vectors via analog-to-digital converters (ADC) and then transferred to the computer to reconstruct the images.

Supporting Information

Supporting Information is available from the Wiley Online Library or from the author.

Acknowledgements

D.Y. and Y.L. contributed equally to this work. This work was supported by National Key R&D Plan (2022YFA1405600), Key Research Project of the Beijing Natural Science Foundation (Grant No. Z210006) and the National Natural Science Foundation of China Youth Science Fund (Grant No. 12104051, 12204035).

Conflict of Interest

The authors declare no conflict of interest.

Data Availability Statement

The data that support the findings of this study are available from the corresponding author upon reasonable request.

Keywords

2D-antiferroelectric materials, $\text{CuBiP}_2\text{Se}_6$, image restoration, neuromorphic computing, optoelectronic synapses

Received: December 7, 2024

Revised: April 14, 2025

Published online:

- [1] C. Kittel, *Phys. Rev.* **1951**, 82, 729.
- [2] X. Hao, J. Zhai, L. B. Kong, Z. Xu, *Prog. Mater. Sci.* **2014**, 63, 0079.
- [3] P. Tolédano, M. Guennou, *Phys. Rev. B* **2016**, 94, 014107.
- [4] R. Xu, K. J. Crust, V. Harbola, R. Arras, K. Y. Patel, S. Prosandeev, H. Cao, Y. T. Shao, P. Behera, L. Caretta, *Adv. Mater.* **2023**, 35, 2210562.
- [5] A. S. Gaur, R. Choudhary, B. Liu, Y. Mudryk, D. Johnson, J. Cui, X. Tan, *Adv. Mater.* **2024**, 36, 2312856.
- [6] H. Bai, J. Wu, X. Su, H. Peng, Z. Li, D. Yang, Q. Zhang, C. Uher, X. Tang, *Nat. Commun.* **2021**, 12, 7207.
- [7] H. Pan, M. Zhu, E. Banyas, L. Alaerts, M. Acharya, H. Zhang, J. Kim, X. Chen, X. Huang, M. Xu, *Nat. Mater.* **2024**, 23, 944.
- [8] T. Hu, Z. Fu, X. Liu, L. Li, C. Xu, Y. Zhou, F. Cao, J. Xia, X. Chen, G. Wang, *Nat. Commun.* **2024**, 15, 9293.
- [9] H. Borkar, V. Singh, B. Singh, M. Tomar, V. Gupta, A. Kumar, *RSC Adv.* **2014**, 4, 22840.
- [10] T. Pan, J. Zhang, Z. N. Guan, Y. Yan, J. Ma, X. Li, S. Guo, J. Wang, Y. Wang, *Adv. Electron. Mater.* **2022**, 8, 2200793.
- [11] H. Qi, R. Zuo, A. Xie, A. Tian, J. Fu, Y. Zhang, S. Zhang, *Adv. Funct. Mater.* **2019**, 29, 1903877.
- [12] G. Ge, C. Shi, C. Chen, Y. Shi, F. Yan, H. Bai, J. Yang, J. Lin, B. Shen, J. Zhai, *Adv. Mater.* **2022**, 34, 2201333.
- [13] R. Cao, X. Zhang, S. Liu, J. Lu, Y. Wang, H. Jiang, Y. Yang, Y. Sun, W. Wei, J. Wang, C. A. N. B. A.-F. Transistor, *Nat. Commun.* **2022**, 13, 7018.
- [14] Z. Lv, H. Wang, J. Cao, C. Zhang, G. Zhao, R. Yu, B. Zhang, X. Xu, Y. Jiang, J. Miao, *Adv. Mater. Interfaces* **2022**, 9, 2201005.
- [15] S. Prosandeev, S. Prokhorenko, Y. Nahas, Y. Yang, C. Xu, J. Grollier, D. Talbayev, B. Dkhil, L. Bellaiche, *Phys. Rev. B* **2022**, 105, L100101.

- [16] F. Xue, Y. Ma, H. Wang, L. Luo, Y. Xu, T. D. Anthopoulos, M. Lanza, B. Yu, X. Zhang, *Matter* **2022**, 5, 1999.
- [17] Y. Ma, Y. Yan, L. Luo, S. Pazos, C. Zhang, X. Lv, M. Chen, C. Liu, Y. Wang, A. Chen, *Nat. Commun.* **2023**, 14, 7891.
- [18] Y. A. Genenko, J. Glaum, M. J. Hoffmann, K. Albe, *Mater. Sci. Eng. B* **2015**, 192, 52.
- [19] S. Hadke, M. A. Kang, V. K. Sangwan, M. C. Hersam, *Chem. Rev.* **2025**, 125, 835.
- [20] H. Li, X. Xiong, F. Hui, D. Yang, J. Jiang, W. Feng, J. Han, J. Duan, Z. Wang, L. Sun, *Nanotechnology* **2022**, 33, 465601.
- [21] L. Sun, H. Yu, D. Wang, J. Jiang, D. Kim, H. Kim, S. Zheng, M. Zhao, Q. Ge, H. Yang, *2D Mater.* **2018**, 6, 015029.
- [22] S. Li, F. Wang, Y. Wang, J. Yang, X. Wang, X. Zhan, J. He, Z. Wang, *Adv. Mater.* **2024**, 36, 2301472.
- [23] A. Simon, J. Ravez, V. Maisonneuve, C. Payen, V. Cajipe, *Chem. Mater.* **1994**, 6, 1575.
- [24] S. A. Tawfik, J. R. Reimers, C. Stampfl, M. J. Ford, *J. Phys. Chem. C* **2018**, 122, 22675.
- [25] J. R. Reimers, S. A. Tawfik, M. J. Ford, *Chem. Sci.* **2018**, 9, 7620.
- [26] E. Durand, G. Ouvrard, M. Evain, R. Brec, *Inorg. Chem.* **1990**, 29, 4916.
- [27] M. A. Gave, D. Bilc, S. Mahanti, J. D. Breshears, M. G. Kanatzidis, *Inorg. Chem.* **2005**, 44, 5293.
- [28] F. Liu, L. You, K. L. Seyler, X. Li, P. Yu, J. Lin, X. Wang, J. Zhou, H. Wang, H. He, *Nat. Commun.* **2016**, 7, 12357.
- [29] T. Li, Y. Wu, G. Yu, S. Li, Y. Ren, Y. Liu, J. Liu, H. Feng, Y. Deng, M. Chen, *Nat. Commun.* **2024**, 15, 2653.
- [30] M. A. Susner, M. Chyasnavichyus, M. A. McGuire, P. Ganesh, P. Maksymovych, *Adv. Mater.* **2017**, 29, 1602852.
- [31] X. Wang, Z. Song, W. Wen, H. Liu, J. Wu, C. Dang, M. Hossain, M. A. Iqbal, L. Xie, *Adv. Mater.* **2019**, 31, 1804682.
- [32] Z. Shang, L. Liu, G. Wang, H. Xu, Y. Cui, J. Deng, Z. Lou, Y. Yan, J. Deng, S. T. Han, *ACS Nano* **2024**, 18, 30530.
- [33] H. Choi, S. Baek, H. Jung, T. Kang, S. Lee, J. Jeon, B. C. Jang, S. Lee, *Adv. Mater.* **2024**, <https://doi.org/10.1002/adma.202406970>.
- [34] J. Bai, D. He, B. Dang, K. Liu, Z. Yang, J. Wang, X. Zhang, Y. Wang, Y. Tao, Y. Yang, *Adv. Mater.* **2024**, 36, 2401060.
- [35] W. F. Io, S.-Y. Pang, L. W. Wong, Y. Zhao, R. Ding, J. Mao, Y. Zhao, F. Guo, S. Yuan, J. Zhao, *Nat. Commun.* **2023**, 14, 7304.
- [36] X. Wang, Z. Shang, C. Zhang, J. Kang, T. Liu, X. Wang, S. Chen, H. Liu, W. Tang, Y. J. Zeng, *Nat. Commun.* **2023**, 14, 840.
- [37] Y. Sun, R. Zhang, C. Teng, J. Tan, Z. Zhang, S. Li, J. Wang, S. Zhao, W. Chen, B. Liu, *Mater. Today* **2023**, 66, 9.
- [38] P. Wang, J. Li, W. Xue, W. Ci, F. Jiang, L. Shi, F. Zhou, P. Zhou, X. Xu, *Adv. Sci.* **2024**, 11, 2305679.
- [39] A. Dziaugys, J. Banyas, J. Macutkevicius, Y. Vysochanskii, I. Pritz, M. Gurzan, *Phase Transitions* **2011**, 84, 147.
- [40] X. Jiang, J. Tan, D. Liu, Y. Feng, K. Q. Chen, E. A. Kazakova, A. S. Vasenko, E. V. Chulkov, *J. Phys. Chem. Lett.* **2024**, 15, 3611.
- [41] W. He, L. Kong, P. Yu, G. Yang, *Adv. Mater.* **2023**, 35, 2209995.
- [42] H. Hu, K. Wang, H. Long, W. Liu, B. Wang, P. Lu, *Nano Lett.* **2015**, 15, 3351.
- [43] C. G. Zhang, W. X. Ji, P. Li, C. W. Zhang, P. J. Wang, *Chem. Phys. Lett.* **2021**, 780, 138933.
- [44] D. Li, J. K. Qin, B. X. Zhu, L. Q. Yue, S. Qiang, C. Y. Zhu, P. Y. Huang, L. Zhen, C. Y. Xu, *Adv. Funct. Mater.* **2025**, 35, 2417619.
- [45] D. Yang, H. Yang, X. Guo, H. Zhang, C. Jiao, W. Xiao, P. Guo, Q. Wang, D. He, *Adv. Funct. Mater.* **2020**, 30, 2004514.
- [46] X. Chen, D. Yang, G. Hwang, Y. Dong, B. Cui, D. Wang, H. Chen, N. Lin, W. Zhang, H. Li, *ACS Nano* **2024**, 18, 10758.
- [47] L. Sun, Y. Zhang, G. Han, G. Hwang, J. Jiang, B. Joo, K. Watanabe, T. Taniguchi, Y. M. Kim, W. J. Yu, *Nat. Commun.* **2019**, 10, 3161.
- [48] H. Li, S. Wang, X. Zhang, W. Wang, R. Yang, Z. Sun, W. Feng, P. Lin, Z. Wang, L. Sun, *Adv. Intell. Syst.* **2021**, 3, 2100017.
- [49] Q. Zhang, Z. Zhang, C. Li, R. Xu, D. Yang, L. Sun, *Chip* **2023**, 2, 100059.
- [50] C. Li, X. Chen, Z. Zhang, X. Wu, T. Yu, R. Bie, D. Yang, Y. Yao, Z. Wang, L. Sun, *Nano Lett.* **2024**, 24, 15025.
- [51] Z. Xie, C. Zhuge, Y. Zhao, W. Xiao, Y. Fu, D. Yang, S. Zhang, Y. Li, Q. Wang, Y. Wang, *Adv. Funct. Mater.* **2022**, 32, 2107314.
- [52] Y. Lin, X. Chen, Q. Zhang, J. You, R. Xu, Z. Wang, L. Sun, *Int. J. Extreme Manuf.* **2024**, 6, 032011.
- [53] Z. Zhang, D. Yang, H. Li, C. Li, Z. Wang, L. Sun, H. Yang, *Neuromorphic Comput. Eng.* **2022**, 2, 032004.
- [54] W. Shin, J. Im, R. H. Koo, J. Kim, K. R. Kwon, D. Kwon, J. J. Kim, J. H. Lee, D. Kwon, *Adv. Sci.* **2023**, 10, 2207661.
- [55] X. Lin, Z. Feng, Y. Xiong, W. Sun, W. Yao, Y. Wei, Z. L. Wang, Q. Sun, *Int. J. Extreme Manuf.* **2024**, 6, 032011.
- [56] Z. Wang, M. Zhang, D. Xie, Z. Liu, G. Li, J. Xie, E. Guo, M. He, C. Wang, G. Yang, *Adv. Electron. Mater.* **2024**, <https://doi.org/10.1002/aelm.202400612>.
- [57] C. W. Lynn, C. M. Holmes, S. E. Palmer, *Nat. Phys.* **2024**, 20, 484.
- [58] Z. Wang, Y. Song, G. Zhang, Q. Luo, K. Xu, D. Gao, B. Yu, D. Loke, S. Zhong, Y. Zhang, *Int. J. Extreme Manuf.* **2024**, 6, 032006.
- [59] L. Sun, Z. Wang, J. Jiang, Y. Kim, B. Joo, S. Zheng, S. Lee, W. J. Yu, B. S. Kong, H. Yang, *Sci. Adv.* **2021**, 7, abg1455.
- [60] Z. Huang, Y. Li, Y. Zhang, J. Chen, J. He, J. Jiang, *Int. J. Extreme Manuf.* **2024**, 6, 032003.
- [61] C. Lu, J. Meng, J. Song, T. Wang, H. Zhu, Q. Q. Sun, D. W. Zhang, L. Chen, *Nano Lett.* **2024**, 24, 1667.
- [62] G. Li, D. Xie, H. Zhong, Z. Zhang, X. Fu, Q. Zhou, Q. Li, H. Ni, J. Wang, E. Guo, *Nat. Commun.* **2022**, 13, 1729.
- [63] T. Li, J. Miao, X. Fu, B. Song, B. Cai, X. Ge, X. Zhou, P. Zhou, X. Wang, D. Jariwala, *Nat. Nanotechnol.* **2023**, 18, 1303.
- [64] G. Feng, X. Zhang, B. Tian, C. Duan, *InfoMat* **2023**, 5, 12473.
- [65] C. Y. Wang, S. J. Liang, S. Wang, P. Wang, Z. a. Li, Z. Wang, A. Gao, C. Pan, C. Liu, J. Liu, *Sci. Adv.* **2020**, 6, aba6173.
- [66] D. Pathak, P. Krahenbuhl, J. Donahue, T. Darrell, A. A. Efros, in *IEEE Conf. on Computer Vision and Pattern Recognition*, IEEE, Piscataway, NJ **2016**, pp. 2536–2544, <https://doi.org/10.1109/CVPR.2016.278>.
- [67] G. Cohen, S. Afshar, J. Tapson, A. Van Schaik, in *Int. Joint Conf. on Neural Networks*, IEEE, Piscataway, NJ **2017**, pp. 2921–2926, <https://doi.org/10.1109/IJCNN.2017.7966217>.
- [68] M. Heusel, H. Ramsauer, T. Unterthiner, B. Nessler, S. Hochreiter, in *Advances in Neural Information Processing Systems*, Curran Associates, New York, NY, **2017**, p. 30.